IB-AS-BS-2019-37

Implementation of a $ln(\omega)$-based SSG/LRR Reynolds Stress Model into the DLR-TAU Code

Sebastian Braun

Institute of Aerodynamics and Flow Technology
$C^2A^2S^2E$

DLR
Deutsches Zentrum für Luft- und Raumfahrt
German Aerospace Center

Bericht des Instituts für Aerodynamik und Strömungstechnik
Report of the Institute of Aerodynamics and Flow Technology

DLR-IB-AS-BS-2019-37

Implementation of a ln(ω)-based SSG/LRR Reynolds Stress Model into the DLR-TAU Code

Sebastian Braun

Herausgeber:
Deutsches Zentrum für Luft- und Raumfahrt e.V.
Institut für Aerodynamik und Strömungstechnik
Lilienthalplatz 7, 38108 Braunschweig

ISSN 1614-7790

Stufe der Zugänglichkeit: 1
Braunschweig, im März 2019

Institutsdirektor:
Prof. Dr.-Ing. habil. C.-C. Rossow
Prof. Dr.-Ing. A. Dillmann

Verfasser:
Dr.-Ing. Sebastian Braun

Abteilung: $C^2A^2S^2E$
Abteilungsleiter:
Prof. Dr.-Ing. Norbert Kroll
Dr.-Ing. Cornelia Grabe

Der Bericht enthält:
39 Seiten
19 Bilder
3 Tabellen
29 Literaturstellen

DLR-IB-AS-BS-2019-37

Implementation of a ln(ω)-based SSG/LRR Reynolds Stress Model into the DLR-TAU Code

Sebastian Braun

Verteiler:

Institutsbibliothek	1 Exemplar
Verfasser/Co-Autoren	1 Exemplar
Institutsleitung	1 Exemplar
Abteilungsleiter	1 Exemplar
Deutsche Bibliothek in Frankfurt/Main	2 Exemplare
Niedersächsische Landesbibliothek Hannover	1 Exemplar
Techn. Informationsbibliothek Hannover	1 Exemplar
Zentralbibliothek BS	1 Exemplar
Zentralarchiv GÖ	1 Exemplar
Reserve	5 Exemplare

Contents

List of symbols **4**

1 Introduction **8**

2 SSG/LRR-$ln(\omega)$-RSM **10**
2.1 $ln(\omega)$-Transport Equation 10
2.2 Boundary Conditions 12
2.3 Limiter 12

3 Verification and Validation **14**
3.1 Wall bounded flows 15
3.1.1 Zero Pressure Gradient Flat Plate 15
3.1.2 2D Fully Developed Channel Flow at High Reynolds Number 17
3.1.3 NACA 0012 Mesh Refinement Study 18
3.2 Separated flows 19
3.2.1 2D Airfoil Near-Wake 19
3.2.2 Axisymmetric Transonic Bump 21
3.2.3 2D Backward facing step 22
3.2.4 2D NASA Wall-mounted Hump 24
3.2.5 DLR-F15 with a Spoiler 25

4 Stability and Robustness **28**
4.1 RAE 2822 28
4.2 2D Airfoil Near-Wake 29
4.3 2D Backward facing step 30
4.4 Common Research Model 31
4.5 DLR-F11 33

5 Summary **35**

Bibliography **39**

List of symbols

Greek symbols

α ..... angle of attack

α ..... coefficient of the SSG/LRR-model

β ..... coefficient of the SSG/LRR-model

δ ..... incident angle of a spoiler

ϵ ..... dissipation rate

μ ..... dynamic viscosity

μ_t ..... eddy viscosity

ω ..... specific dissipation rate

$\hat{\omega}$ ..... natural logarithm of the specific dissipation rate

ϕ ..... arbitrary model coefficient or variable

ρ ..... density

σ ..... coefficient of the SSG/LRR-model

ζ ..... argument of the F_1-blending function

Subscripts

i, j, k ..... indices of the Einstein notation

$\hat{\omega}$ ..... variable or function of the $In(\omega)$-equation

ω ..... variable or function of the ω-equation

∞ ..... reference value

w ..... value on a (viscous) wall

Superscripts

$\bar{}$ ..... Favre averaging

$\tilde{}$ ..... Reynolds averaging

Roman Symbols

C_μ ..... model coefficient

c_d ..... drag coefficient

c_f ..... skin friction coefficient

c_L ..... lift coefficient

c_m ..... pitching moment coefficient

c_p ..... pressure coefficient

d ..... wall distance

F ..... extrapolation factor

F_1 ..... blending function

g ..... length-scale providing variable of the SSG/LRR-g model

k ..... turbulence kinetic energy

G ..... additional gradient term

H ..... height of a geometry

M ..... Mach number

N ..... number of grid points

P ..... production term

R ..... Reynolds stress tensor

Re ..... Reynolds number

$Rrho$ ..... residual of the density

$Rrhor11$ ..... residual of the first normal component of the Reynolds stress tensor

$Rrhorg$ ..... residual of the length-scale providing variable g

$RrhorInw$ ..... residual of the natural logarithm of the specific dissipation rate $\hat{\omega}$

$Rrhorw$ ..... residual of the specific dissipation rate ω

Tu ..... turbulence level

t ..... time

U, v ..... velocities

u^+ ..... friction velocity

x ..... cartesian coordinate

y ..... cartesian coordinate

y^+ ..... dimensionless distance to the nearest wall / wall units

z ..... cartesian coordinate

Abbreviations

AIAA ..... **A**merican **I**nstitute of **A**eronautics and **A**stronautics

CFD ..... **C**omputational **F**luid **D**ynamics

CRM ..... **C**ommon **R**esearch **M**odel

DG ..... **D**iscontinuous-**G**alerkin

DLR ..... **D**eutsches Zentrum für **L**uft- und **R**aumfahrt

EARSM ..... **E**xplicit **A**lgebraic **R**eynolds **S**tress **M**odel

EVM ..... **E**ddy **V**iscosity **M**odel

LOTW ..... law-**o**f-**t**he-**w**all

LRR ..... **L**aunder **R**eece **R**odi

LUSGS ..... **l**ower-**u**pper **S**ymmetric **G**auss-**S**eidel

MG ..... **m**ulti**g**rid

NASA ..... **N**ational **A**eronautics and **S**pace **A**dministration

RSM ..... **R**eynolds **S**tress **M**odel

SA ..... **S**palart-**A**llmaras

SG ..... **s**ingle**g**rid

SSG ..... **S**peziale **S**arkar **G**atski

SST ..... **S**hear **S**tress **T**ransport

TMR ..... **T**urbulence **M**odeling **R**esource

VitAM ..... Advanced Aircraft Understanding via the **Vir**t**u**al **A**ircraft **M**odel

1 Introduction

In contemporary aircraft design processes, the used Computational fluid dynamics (CFD) methods rely on the Reynold-averaged Navier-Stokes-equations and some type of turbulence modelling in most cases. However, the accuracy of widespread eddy-viscosity models (EVM) like the Spalart-Allmaras (SA) model [26] or the shear-stress transport model (SST) published by Menter [21] seem to be insufficient at the borders of the flight envelope where massive flow separation dominates flight physics. On the contrary, dropping the Boussinesq hypothesis used in EVMs and modelling the transport equations for the Reynolds stresses directly allows for a better description of flow physics. Though, these so called Reynolds stress models (RSM) are often reported to be hard to solve and to degenerate the robustness and stability of the solution process in comparison to state of the art EVMs. Nevertheless, the SSG/LRR-ω-RSM developed by Eisfeld [11] has been demonstrated to be applicable to a wide range of aeronautical flow problems [14, 7, 8, 6] and is now routinely used within DLR and industry for fairly complex cases. However, stability and robustness issues remain a problem especially in more complex cases like high-lift configurations for example. In order to improve the robustness, Togiti and Eisfeld [27] developed the so called SSG/LRR-g model, where the transport equation of the specific dissipation rate ω is replaced by a transport equation for $g = 1/\sqrt{\omega}$. This new variant of the model no longer suffers from the singular behavior of ω and the lack of a natural boundary condition on viscous walls. Furthermore, users of the DLR-TAU code reported that the g-formulation of the SSG/LRR-RSM is far more stable than the original model in many cases. Due to these advantages, the SSG/LRR-g has become the "standard"-RSM in the TAU code for most applications.

In this report, an additional formulation of the SSG/LRR-RSM is presented in which the specific dissipation rate ω is replaced by its natural logarithm. This transformation based on ideas of Bassi et al. [2] that were developed in order to make the Wilcox-k-ω model [29] manageable for solvers based on a Discontinuous-Galerkin (DG) discretization. Using the logarithmically transformed equation solves two main problems that arise in the context of DG discretization:

1. The extremely large slope of ω near viscous walls[1] is alleviated. Therefore, the length-scale determining variable can be much better represented with the polynomial ansatz functions DG methods inherently rely on.

2. Within the transformed equation, the new length-scale providing variable only appears in the exponent of the Euler number. This removes the necessity of a numerical limitation of the variable that is required in the original formulation in order to fulfill energy stability requirements[2] and cannot be enforced in a DG method directly.

In flow solvers based on a finite volume approach like the DLR-TAU code, the problem of negative length-scales is fixed in most cases by using a numerical or physical limiter that enforces positive values subsequent of each iteration step and guarantees that the energy stability requirements are fulfilled in the next iteration step. However, it is assumed that these inevitable supplementary changes of values also introduce instabilities into the solution procedure. Therefore, the idea of a logarithmic transport variable is transferred to the length-scale determining transport equation of the SSG/LRR-ω-RSM in order to improve the robustness of the solution procedure in TAU. It has to be mentioned, that this modification only removes the necessity of limiting the length-scale determining variable. The realizability[3] of the Reynolds-stress tensor still has to be enforced by a limiter. Furthermore, a logarithmically transformed ω-equation still suffers from the lack of a natural boundary condition on viscous walls and the necessity of extrapolating values from the flow field onto the wall. However, the magnitude of the extrapolated values is extremely reduced. In computations that use the SSG/LRR-ω model, the specific dissipation rate increases from values near zero outside of the boundary layer to values that are very often bigger than several trillions[4] onto a viscous wall. After logarithmizing the equation, the values on a viscous wall remain always smaller than three orders of magnitude. This may improve the robustness of the implicit backward Euler solver used in TAU where large linear systems are solved using a LUSGS-scheme that may become stiff in cases where the magnitude of the entries in the matrices varies to widely.

In the subsequent chapter 2, the formulation of the new SSG/LRR-$ln(\omega)$ model version will be presented. In chapter 3, the implementation of the model in the flow solver TAU will be verified and the model will be validated using several test cases. The results of stability and performance tests with the new model can be found in chapter 4 and a short summary will be given in chapter 5.

[1] The values of ω depend on the distance d to the viscous wall and increase with $1/d^2$ towards the wall.
[2] Refer [1] or [4] for details.
[3] The normal components of the Reynolds stress tensor have to be positive and the off-diagonal components have to fulfill the Schwarz inequality (ref. chapter 2.3).
[4] The exact order of magnitude of the values on the wall is case dependent and varies with the grid resolution near the wall and the viscosity of the fluid (ref. equation 2.13).

2 SSG/LRR-$ln(\omega)$-RSM

In this chapter, the new $ln(\omega)$-variant of the SSG/LRR-RSM is derived from the original SSG/LRR-ω model by transferring the ideas by Bassi et al. [2] from the Wilcox-k-ω model to the length-scale equation of the SSG/LRR-ω model. Furthermore, boundary conditions for the new length-scale determining variable $ln(\omega)$ and the remaining requirements for numerical limitations are given.

2.1 $ln(\omega)$-Transport Equation

Compared to the original SSG/LRR-ω model, the modified model is unchanged besides the length-scale determining transport equation. There, the specific dissipation rate ω is replaced by the natural logarithm of this quantity that will be referred as $\hat{\omega}$ throughout this report:

$$\hat{\omega} = ln(\omega)\,. \tag{2.1}$$

The corresponding transport equation for $\hat{\omega}$ results directly from

$$\frac{D\hat{\omega}}{Dt} = \frac{D\hat{\omega}}{D\omega}\frac{D\omega}{Dt} = \frac{\partial\hat{\omega}}{\partial\omega}\frac{D\omega}{Dt} = \frac{1}{e^{\hat{\omega}}}\frac{D\omega}{Dt}, \tag{2.2}$$

using $\partial\hat{\omega}/\partial\omega = 1/\omega$ and $\omega = e^{\hat{\omega}}$.

After multiplying the ω-equation with $1/e^{\hat{\omega}}$ and substituting ω for $e^{\hat{\omega}}$, the transformed transport equation for the new transport variable $\hat{\omega}$ reads[1]

$$\begin{aligned}\frac{\partial\bar{\rho}\hat{\omega}}{\partial t} + \frac{\partial\left(\bar{\rho}\hat{\omega}\tilde{U}_k\right)}{\partial x_k} =& \frac{\alpha_{\hat{\omega}}}{\tilde{k}}\frac{\bar{\rho}P_{kk}}{2} - \beta\bar{\rho}e^{\hat{\omega}} + \frac{\partial}{\partial x_k}\left[\left(\mu + \sigma_{\hat{\omega}}\frac{\bar{\rho}\tilde{k}}{e^{\hat{\omega}}}\right)\frac{\partial\hat{\omega}}{\partial x_k}\right] \\ &+ \underbrace{\left(\mu + \sigma_{\hat{\omega}}\frac{\bar{\rho}\tilde{k}}{e^{\hat{\omega}}}\right)\frac{\partial\hat{\omega}}{\partial x_k}\frac{\partial\hat{\omega}}{\partial x_k}}_{G^{(\hat{\omega})}} + \sigma_d\frac{\bar{\rho}}{e^{\hat{\omega}}}max\left(\frac{\partial\tilde{k}}{\partial x_k}\frac{\partial\hat{\omega}}{\partial x_k}, 0\right),\end{aligned} \tag{2.3}$$

[1] The additional gradient term $G^{(\hat{\omega})}$ arises from the transformation of the diffusion term and acts as a source of $\hat{\omega}$ in the equation.

in which $\bar{\rho}P_{kk}$ is computed from the turbulence production term

$$\bar{\rho}P_{ij} = -\bar{\rho}\tilde{R}_{ik}\frac{\partial \tilde{U}_j}{\partial x_k} - \bar{\rho}\tilde{R}_{jk}\frac{\partial \tilde{U}_i}{\partial x_k} \tag{2.4}$$

and the specific kinetic turbulence energy $\tilde{k}$ is half the trace of the Reynolds stress tensor R_{ii}:

$$\tilde{k} = \frac{\tilde{R}_{ii}}{2}. \tag{2.5}$$

The model coefficients $\phi = \alpha_{\hat{\omega}}, \beta_{\hat{\omega}}, \sigma_{\hat{\omega}}, \sigma_d$ are blended similar to the SST model and the original SSG/LRR-ω RSM via

$$\phi = F_1\phi^{(\hat{\omega})} + (1 - F_1)\,\phi^{(\epsilon)} \tag{2.6}$$

and the F_1-blending function

$$F_1 = tanh\left(\zeta^4\right). \tag{2.7}$$

The argument ζ of the blending function results from

$$\zeta = min\left[max\left(\frac{\sqrt{\tilde{k}}}{C_\mu e^{\hat{\omega}} d}, \frac{500\bar{\mu}}{\bar{\rho}e^{\hat{\omega}}d^2}\right), \frac{4\sigma_{\hat{\omega}}^{(\epsilon)}\bar{\rho}\tilde{k}e^{\hat{\omega}}}{\sigma_d^{(\epsilon)}\bar{\rho}d^2 max\left(\frac{\partial\tilde{k}}{\partial x_k}\frac{\partial\hat{\omega}}{\partial x_k}, 0\right)}\right] \tag{2.8}$$

depending on the wall distance d and the model coefficient $C_\mu = 0.09$.

The bounding values $\phi^{(\epsilon)}$ and $\phi^{(\hat{\omega})}$ of the blended model coefficients are listed in table 2.1. Again, there are no changes compared to the original formulation of the SSG/LRR-RSM.

	$\alpha_{\hat{\omega}}$	$\beta_{\hat{\omega}}$	$\sigma_{\hat{\omega}}$	σ_d
$\phi^{(\epsilon)}$	0.44	0.0828	0.856	1.712
$\phi^{(\hat{\omega})}$	0.5556	0.075	0.5	0

Table 2.1: Bounding values of the coefficients of the SSG/LRR-model [12]

All other transport equations of the SSG/LRR model remain unchanged. They are coupled to the $\hat{\omega}$-transport equation by using the isotropic dissipation rate ϵ that is computed as follows:

$$\epsilon = C_\mu \tilde{k} e^{\hat{\omega}}. \tag{2.9}$$

2.2 Boundary Conditions

At far field boundaries, the length-scale determining variable $\hat{\omega}$ is computed as

$$\hat{\omega}_\infty = In\left(\frac{\bar{\rho}_\infty \tilde{k}_\infty}{\mu_{t,\infty}}\right), \tag{2.10}$$

where the equivalent eddy viscosity $\mu_{t,\infty}$ is expressed in terms of a user defined fraction $f^{(\bar{\mu}_\infty)}$ of the molecular viscosity $\bar{\mu}_\infty$ of the fluid at the far field:

$$\mu_{t,\infty} = f^{(\bar{\mu}_\infty)} \cdot \bar{\mu}_\infty. \tag{2.11}$$

The specific turbulence kinetic energy $\tilde{k}_\infty$ at the far field is computed from the user-defined far field turbulence level Tu_∞ and the inflow velocity U_∞:

$$\tilde{k}_\infty = \frac{3}{2}\left(Tu_\infty \cdot U_\infty\right)^2 \tag{2.12}$$

On viscous walls, the well-known approach by Menter [21] is used that extrapolates the value of the nearest field point onto the wall. In order to get the correct values for $\hat{\omega}$, the original equation is logarithmized:

$$\hat{\omega}_w = In\left(F\frac{6\bar{\mu}_w}{\bar{\rho}_w \beta_{\hat{\omega}}^{(\hat{\omega})} d_1^2}\right). \tag{2.13}$$

In Eq. 2.13, d_1 represents the distance between the wall point and the nearest field point and the extrapolation factor is $F = 10$ consistently to reference [12]. The value of $\beta_{\hat{\omega}}^{(\hat{\omega})}$ can be found in table 2.1.

The boundary conditions for the components of the Reynolds stress tensor remain unchanged and can also be found in [12].

2.3 Limiter

As can be seen in equation 2.3 and equation 2.8, the length-scale determining variable $\hat{\omega}$ always appears in the exponent of the Euler number. Therefore, the sign of the source terms as well as the sign of the diffusion coefficient remain unchanged regardless of the

value of $\hat{\omega}$ and no limitation is required to ensure the energy stability requirements. Nevertheless, precautions for the Reynolds stresses have to be made in form of an enforced realizability condition. The diagonal components R_{ii} of the Reynolds stress tensor are limited to a user-defined fraction $f^{(R_\infty)}$ of the far field value $\tilde{k}_\infty$ of the specific turbulence kinetic energy:

$$R_{ii} \geq f^{(R_\infty)} \cdot \frac{2}{3}\tilde{k}_\infty. \tag{2.14}$$

The off-diagonal elements R_{ij} of the Reynolds stress tensor have to fulfill the Schwarz inequality[2]:

$$\left|R_{ij}\right| \leq \sqrt{R_{ii} \cdot R_{jj}}. \tag{2.15}$$

[2]Note that the Einstein summation on i and j is not applied here.

3 Verification and Validation

Here, the term "verification" refers to the examination of the correctness of a model formulation and its error-free implementation into a CFD-code. In this chapter, the objective is to verify if the new $In(\omega)$-variant of the SSG/LRR-RSM that was implemented in the flow solver TAU delivers identical predictions compared to results computed with the original model variant (SSG/LRR-ω) as well as with its derivative SSG/LRR-g on sufficiently refined grids. In particular, test cases for wall bounded flows as well as for separated flows are investigated. Furthermore, the performance of the SSG/LRR-In(ω) model variant is examined by comparing the predictions to experimental data for a subset of these test cases. In the verification and validation study, the subsequent test cases are considered. Besides the DLR-F15 spoiler, all these test cases can be found on the NASA TMR website [25].

- Wall bounded flows:
  - Zero pressure gradient flat plate
  - 2D fully developed channel flow
  - NACA 0012 mesh refinement study
- Separated flows:
  - 2D Airfoil near-wake[1]
  - Axisymmetric transonic bump
  - Backward facing step[1]
  - NASA wall-mounted hump[1]
  - DLR-F15 spoiler[1]

[1] Validation test case

3.1 Wall bounded flows

3.1.1 Zero Pressure Gradient Flat Plate

The zero pressure gradient flat plate represents one of the most basic test cases for turbulence model verification and validation. This test case runs at an inflow Mach number of $M_\infty = 0.2$ and at a Reynolds number of $Re = 5 \cdot 10^6$ based on a reference length of 1 meter. The finest mesh available from the NASA TMR website [25] is used to compare the results computed using the original SSG/LRR-ω model as well as the g-version of this model with results derived with the new SSG/LRR-ln(ω) model variant. Figure 3.1 shows dimensionless velocity profiles of the boundary layer near the surface of the plate at two positions, namely at $x = 0.9$ and $x = 1.9$. Furthermore, the dimensionless Reynolds stress component R_{11} at both positions is shown.

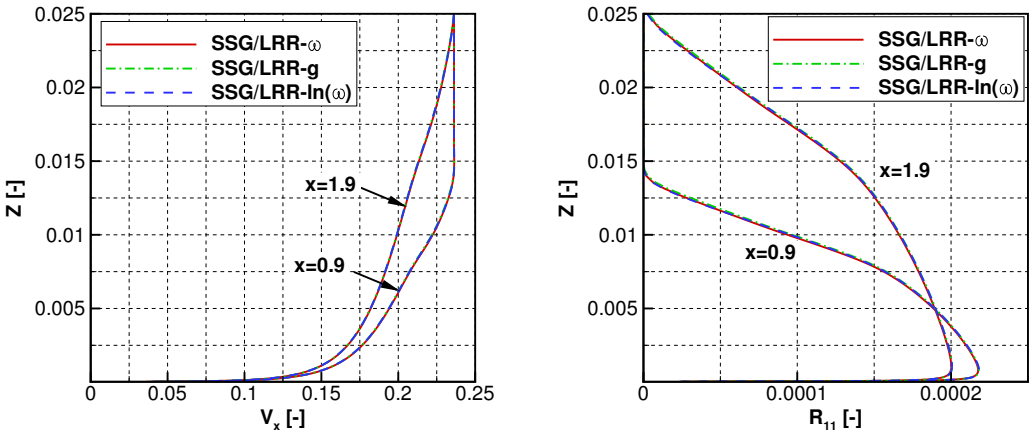

Figure 3.1: Velocity profile (left) and distribution of the Reynolds stress component R_{11} (right) on a flat plate at $x = 0.9$ and $x = 1.9$. Computations conducted with three different versions of the SSG/LRR-RSM at $Re = 5 \times 10^6$ and $M_\infty = 0.2$. All plotted values are non-dimensional.

As can be seen, all three model formulations deliver almost indistinguishable velocity profiles at both positions. Small deviations between the three model versions can be found in the computed Reynolds stresses at the edge of the boundary layer at $x = 1.9$ and $z \approx 0.023$ as well as at $x = 0.9$ and $z \approx 0.012$. It is assumed that these deviations are caused by the used mesh that is not fine enough to resolve the steep gradients occurring in these regions. However, finer meshes are not available to prove this assumption.

Figure 3.2 shows the skin-friction coefficient $c_{f,x}$ on top of the surface of the plate. All three formulations of the SSG/LRR-RSM deliver almost identical results for $x > 0.02$ but large deviations are noticeable at the leading edge of the flat plate as can be seen in the logarithmically scaled plot in the right part of figure 3.2.

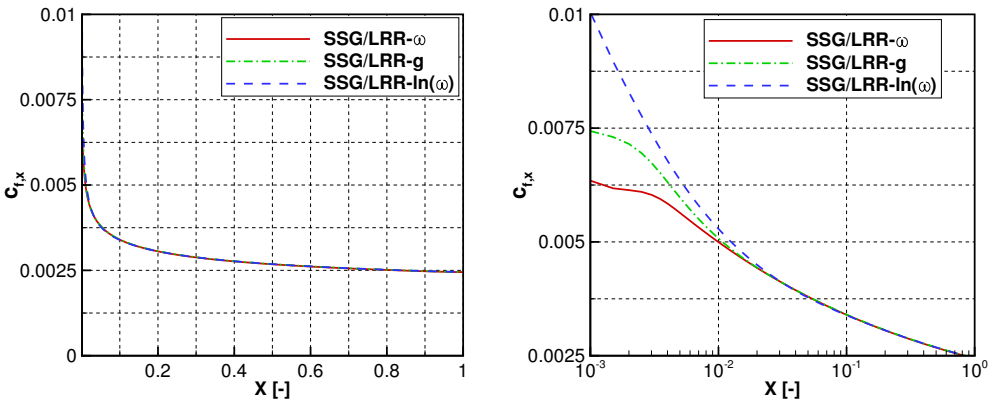

Figure 3.2: Distribution of the skin friction coefficient $c_{f,x}$ on the surface of a flat plate without pressure gradients computed with three different versions of the SSG/LRR-RSM.

This error is caused by the numerical setup of the simulation in which the viscous surface of the plate is directly connected to a symmetry plane. Amongst others, this leads to the unphysical solutions of the Reynolds stresses that are shown in figure 3.3 and creates the deviations in the skin-friction coefficients subsequently. However, this is a known problem of this test case and the aforementioned deviations are not related to the model implementation most likely. Furthermore, the new ln(ω)-formulation seems to be less affected by this numerical problem than the two other versions of the SSG/LRR-model.

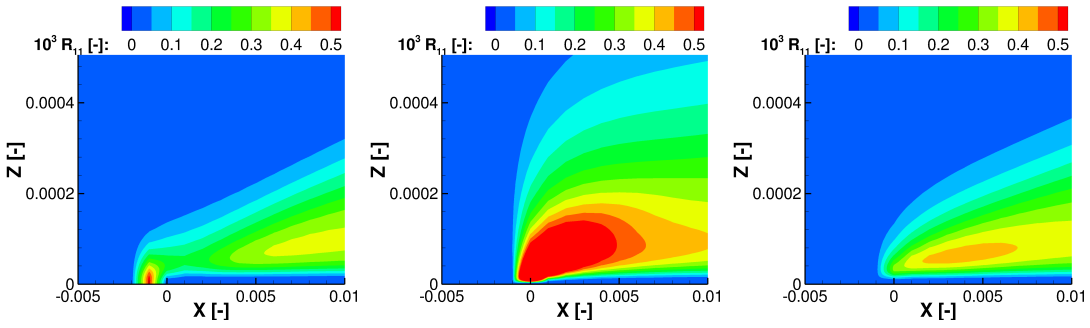

Figure 3.3: Non-dimensional Reynold stress component R_{11} around the intersection between the symmetry plane and the viscous wall of the flat plate at $x = 0.0$. Left: SSG/LRR-ω , center: SSG/LRR-g , right: SSG/LRR-ln(ω) .

3.1.2 2D Fully Developed Channel Flow at High Reynolds Number

The second test case computed here is the 2D fully developed channel flow at a high Reynolds number. The objective of this test case is to examine if the law-of-the-wall (LOTW) for velocities is correctly predicted and to rule out unexpected errors due to the variable transformation from ω to ln(ω). The investigations are carried out at a Reynolds number of $Re_H = 80 \cdot 10^6$ based on the height of the channel H and at a reference Mach number of $M_\infty = 0.2$. The finest grid (161 $\times$ 513 points) available on the NASA Turbulence Modeling Resource website [25] is used for this investigation. The boundary conditions at the inflow and the outflow as well as at the walls of the channel are prescribed as recommended on NASA's TMR website [25].

In figure 3.4 (left), the profile of the skin-friction velocity u^+ in the vicinity of the channel wall extracted at the position $x/H = 500$ is shown in wall units (y^+). The velocity profile delivered by the SSG/LRR-ln(ω) model version is in agreement with the law-of-the-wall in the logarithmic region ($log_{10}(y^+) \approx 4.0 \pm 2.0$) and does not diverge from the velocity profile computed with the original SSG/LRR-ω model. In the right part of figure 3.4, the surface skin-friction coefficient c_f in flow-direction along the channel wall is shown. The c_f-distribution predicted by the SSG/LRR-ln(ω) model version is in close range to the results delivered by the SSG/LRR-ω model. However, the level in the logarithmic region of the boundary layer is marginally higher.

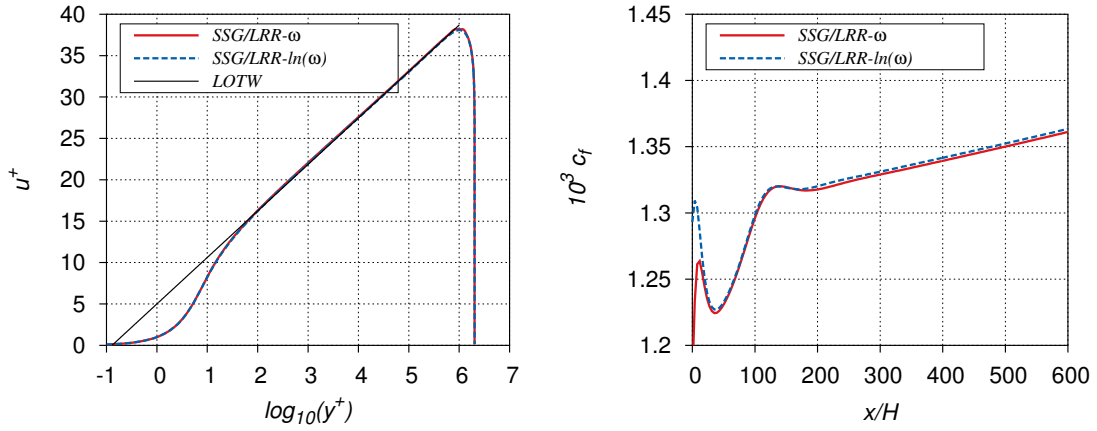

Figure 3.4: Skin-friction velocity distribution (u^+) in wall units (y^+) at $x/H = 500$ (left) and surface skin-friction c_f along the wall (right) for the channel flow computed on the finest grid available from the TMR website [25] at $Re_H = 80 \cdot 10^6$ and $M_\infty = 0.2$.

Based on the results for this test case, it can be stated that the new model variant predicts the velocity profile in a boundary layer correctly and the law-of-the wall for the velocities is fulfilled. The small deviations occurring in the c_f -distribution are most likely caused by discretization errors and not by an incorrect implementation of the model. All in all, the observed deviations seem to be negligible.

3.1.3 NACA 0012 Mesh Refinement Study

In order to investigate the effects of the spatial discretization in more detail, a mesh refinement study is conducted using the well-known NACA 0012 airfoil [20]. For this test case, large numbers of meshes are available with resolutions ranging from a few thousand grid points up to several million points. As the ln(ω)-variant is obtained by a pure mathematical transformation of the SSG/LRR-ω model, both versions are expected to deliver identical results in the limit of infinitely refined meshes. The flow conditions used in this study are a small subsonic reference Mach number of $M_\infty = 0.15$ and a chord based Reynolds number of $Re = 6 \cdot 10^6$. The angle of attack is set to $\alpha = 10°$. Figure 3.5 shows the lift coefficient c_L as well as the drag coefficient c_d plotted versus the number of grid points N for different spatial mesh resolutions. Starting with an initial mesh that consists of barely 29.152 grid points, the number of points is quadrupled in each refinement step. This leads to a final resolution of 29.4 million grid points after five refinement steps. Large deviations of the generated lift and drag can be found on the coarse meshes when the SSG/LRR-ln(ω) model variant is used instead of the original formulation of the equations. However, these deviations vanish with an increasing number of grid points and the results delivered by both SSG/LRR-variants become almost undistinguishable on the finest mesh as expected for correctly implemented models.

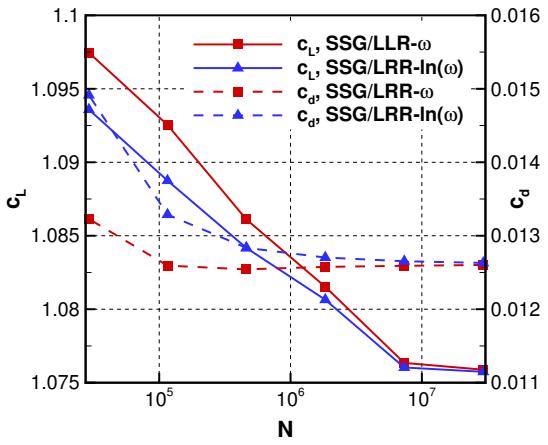

Figure 3.5: Mesh refinement study for lift and drag coefficients using the NACA 0012 airfoil. The meshes are provided by NASA on the TMR-website [25]. The mesh resolution is ranging from $N = 29\,152$ grid points to $N = 29.4$ million points.

3.2 Separated flows

3.2.1 2D Airfoil Near-Wake

As a first test case for separated flows, the wake of the Nakayama airfoil [23] is investigated. The computations are performed at a chord based Reynolds number of $Re_c = 1.2 \cdot 10^6$, a reference Mach number of $M_\infty = 0.088$ and an incidence angle of $\alpha = 0°$. For the current investigation, two grids with two different far field extensions, but with an identical grid resolution in the near field, are used. In one grid, the far field is located 20 chord length c away from the airfoil, while in the other grid, the far field is moved from 20 c to 500 c by adding more grid points. In this way, it is ensured that both grids have the same near field resolution in flow direction up to 20 c. The grid with a far field offset of 20 c has a spatial resolution of 513×225 points while the grid with a far field extension of 500 c has a resolution of 1121×193 points. These resolutions correspond to the second finest meshes available on the NASA TMR website [25].

The objective of the investigations conducted here is to verify that there is no significant influence of the decay rate of ln(ω) on the predictions, in particular on the velocities and the Reynolds shear stress profiles in the wake of the airfoil. For this test case, reference results computed by using the SSG/LRR-ω model are not available as these computations crash on the employed grids. Therefore, the predictions of the newly implemented SSG/LRR-ln(ω) version are compared to results computed by using the SSG/LRR-g model variant. In figure 3.6, the distribution of the velocity component in flow-direction u normalized with the reference velocity U_∞ as well as the Reynolds shear stress profiles $u'v'$ normalized by using the square of the reference velocity U_∞ are shown. These data are extracted at six positions ranging from $x/c = 1.01$ to $x/c = 2.19$ downstream of the trailing edge (located at $x/c = 1.0$) of the airfoil. Overall, the predictions of the ln(ω)-version and the g-variant of the SSG/LRR model are identical on both grids. Neither an influence of the far field distance nor an influence of the turbulence model variant on the decay of the wake can be observed. Furthermore, all results agree well with the experimental data for the streamwise velocity distributions and the Reynolds shear stress profiles.

In addition to the data shown in figure 3.6, the drag- and lift-coefficients are listed in table 3.1 for the SSG/LRR-ln(ω) version and the SSG/LRR-g variant. Furthermore, results computed with the original SSG/LRR-ω model are given. These results were computed with NASAs CFL3D-code and are published on the TMR-website [25]. Again, no significant deviations can be found.

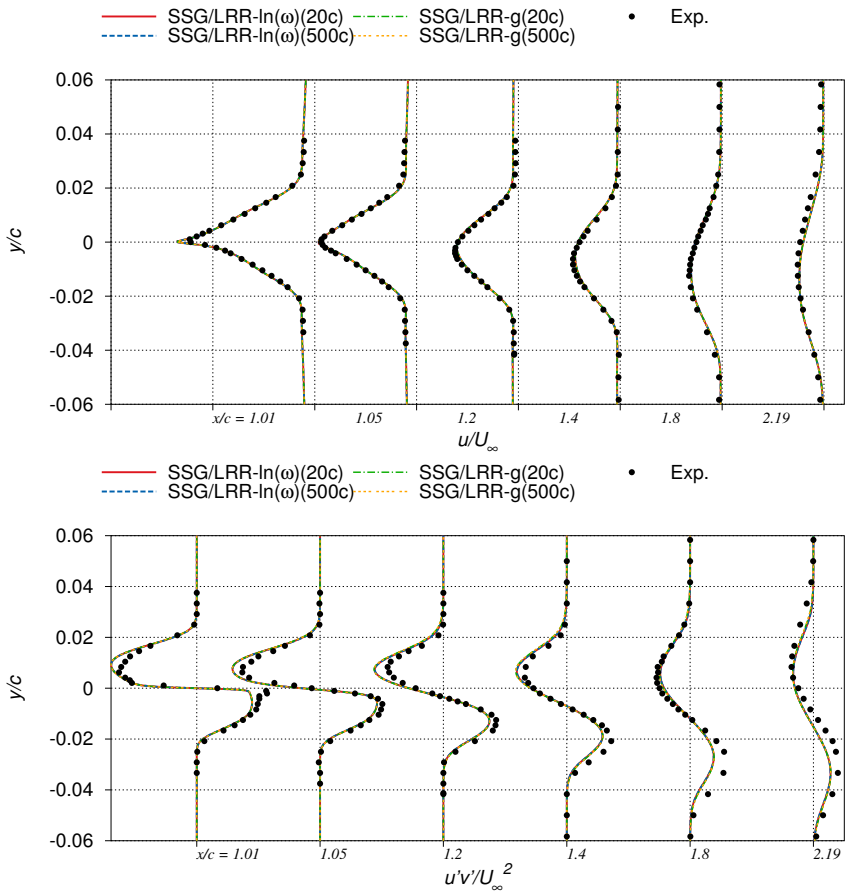

Figure 3.6: Streamwise velocity profiles u/U_∞ and Reynolds shear stress profiles $u'v'/U_\infty^2$ downstream of the Nakayama airfoil. Flow conditions: $Re_c = 1.2 \times 10^6$, $M_\infty = 0.088$, $\alpha = 0°$. Computed on the second finest grid available from the NASA TMR-website [25].

SSG/LRR-variant	$c_L(20c)$	$c_L(500c)$	$\Delta c_L(\%)$	$c_d(20c)$	$c_d(500c)$	$\Delta c_d(\%)$
ω	0.15680	-		0.01014	-	
g	0.15500	0.15559	0.38	0.01031	0.01027	0.39
$ln(\omega)$	0.15504	0.15565	0.39	0.01028	0.01023	0.49

Table 3.1: Force coefficients computed for the Nakayama airfoil at $Re_c = 1.2 \times 10^6$, $M_\infty = 0.088$, $\alpha = 0°$. The meshes and the results for the SSG/LRR-ω model were taken from [25].

3.2.2 Axisymmetric Transonic Bump

The axisymmetric transonic bump test case has been chosen in order to investigate the behavior of the SSG/LRR-ln(ω) implementation in cases where shocks occur. Furthermore, a flow separation can be found in this test case that allows a validation of the new model variant for separating and reattaching flows. A more detailed investigation for such flow types will be conducted in the framework of the test cases "2D Backward Facing Step" and "2D NASA Wall-mounted Hump" that are descripted in the subsequent sections 3.2.3 and 3.2.4. In the axisymmetric bump test case, the shock is induced by the bump that accelerates the flow from a subsonic Mach number of $M_\infty = 0.876$ at the inflow of the domain to supersonic speeds on top of the bump. The boundary layer separates due to the large pressure gradients caused by the shock and creates a separation bubble in the wake of the bump as shown in figure 3.7. In order to create references for the SSG/LRR-ln(ω) model variant, complementary computations with the original SSG/LRR-ω model as well as with the g-version of this model are conducted. The computations are performed at a Reynolds number of $Re = 2.76 \cdot 10^6$ on a grid that contains 721×321 points. Like in the preceding test cases, this grid as well as additional information about the applied boundary conditions can be found on the NASA TMR-website [25].

As can be seen in figure 3.8, almost identical pressure distributions are computed by the three model versions on this grid. Solely downstream of the hump, where the flow is fully

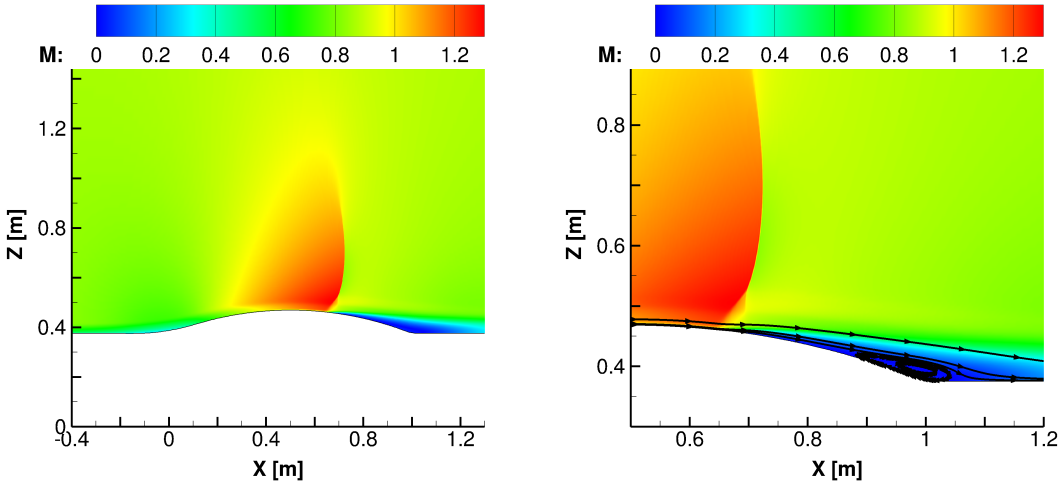

Figure 3.7: Distribution of the Mach number M on top of the axisymmetric bump. Computations conducted at $M_\infty = 0.876$ and $Re = 2.76 \cdot 10^6$ with the SSG/LRR-ln(ω) model on the second finest grid available from the NASA TMR-website [25].

separated, small deviations between the results obtained with the three model versions can be found. The points where the flow separates from the bump as well as the reattachment points can also be found at almost identical positions in all three computations. Larger deviations exist merely in the distributions of the skin friction coefficient c_f plotted in the right part of figure 3.8. However, it is assumed that these deviations are caused by an insufficient resolution of the used mesh and not by an incorrect implementation of the new model version. This assumption is backed by the fact that the results computed with the original SSG/LRR-ω model are in better agreement with the results obtained by using the new SSG/LRR-ln(ω) model version than with the results computed by the well verified SSG/LRR-g model variant.

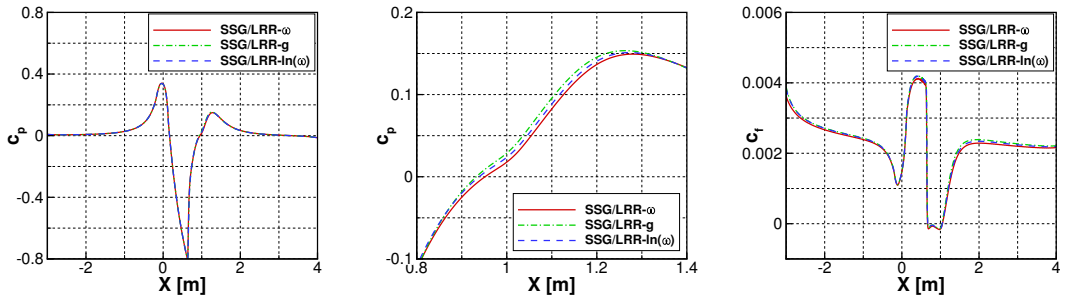

Figure 3.8: Pressure coefficients c_p (left, middle) and skin-friction coefficients c_f (right) on the surface of the axisymmetric bump. Computations conducted at $M = 0.876$ and $\mathrm{Re} = 2.76 \cdot 10^6$ on the second finest grid available from the NASA TMR-Website [25].

3.2.3 2D Backward facing step

In the case of the backward facing step [10], the oncoming flow separates due to the sudden change in the geometry and reattaches at the wall downstream of the step. In this study, computations are carried out at a Reynolds number based on the height of the step H of $Re_H = 36\,000$ and a reference Mach number of $M_\infty = 0.128$ on the second finest grid available on the NASA TMR-website [25]. In contrast to the axisymmetric bump test case, the flow remains completely subsonic in the whole domain. More detailed information about the geometry can be found in [10], information concerning the applied numerical setup and boundary conditions in [25].

In the upper two sections of figure 3.9, the distribution of the pressure coefficient c_P and the skin-friction coefficient c_f along the back-step wall delivered by the new SSG/LRR-ln(ω) model variant are compared to results computed with the SSG/LRR-ω model. In addition, experimental data are shown. Again, both model versions deliver identical c_P-distributions

while small negligible deviations can be found in the c_f-distribution. The main features of the flow that were measured in the experiment like the length of the separation bubble and the reattachment point for example are well captured. In the lower two sections of figure 3.9, the normalized velocity profiles u/U_∞ and the normalized distribution of the Reynolds-stress component $u'v'/U_\infty^2$ measured at one position upstream of the edge of the step as well as at four additional positions downstream of the step can be found. Again, results delivered by both model variants for both quantities are indistinguishable indicating that the new model version has been implemented correctly into the flow solver.

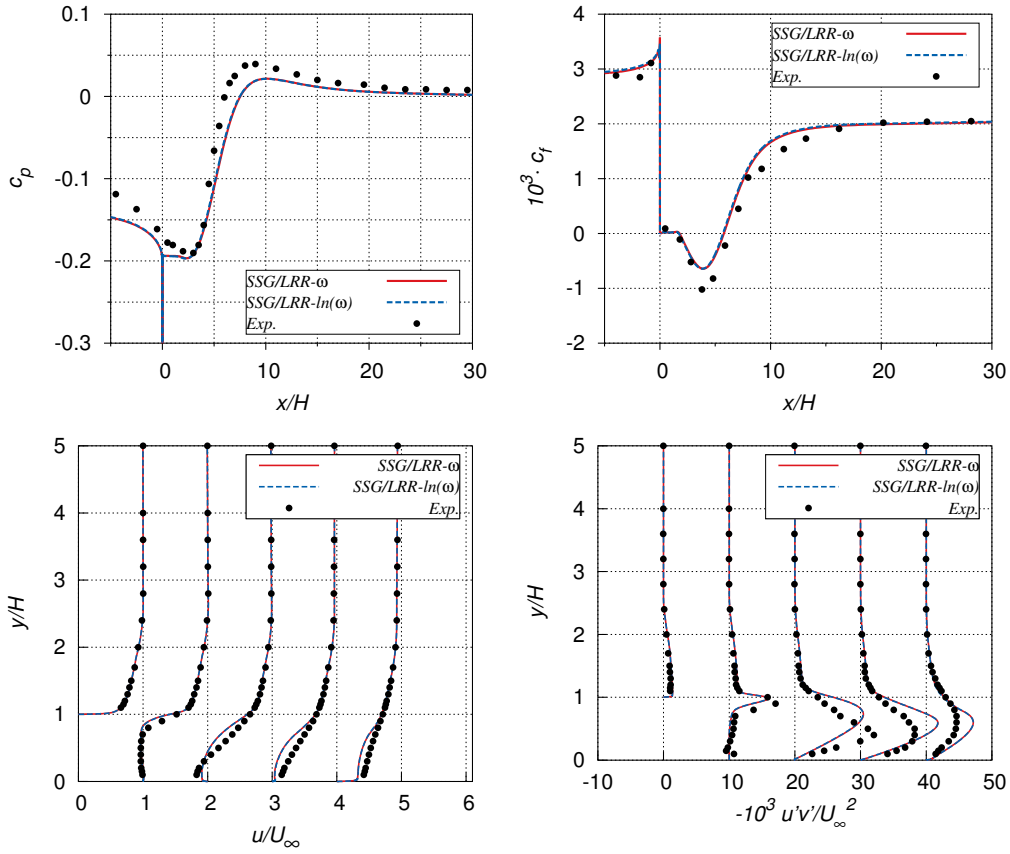

Figure 3.9: Comparison of the pressure distribution c_P and the distribution of the skin-friction coefficient c_f (upper sections) computed with different variants of the SSG/LRR-RSM at the backward facing step. Velocity profiles u and distributions of the Reynolds-stress component $u'v'$ are given for five different positions in the lower section: from left to right: $x/H = -4; 1; 4; 6; 10$. Computations conducted at $M_\infty = 0.128$ and $Re_H = 36\,000$ on the second finest grid available from the NASA TMR-website [25].

3.2.4 2D NASA Wall-mounted Hump

In the wall-mounted hump test case, the oncoming flow separates on the hump due to an adverse pressure gradient imposed to the flow [16]. The computations are carried out at a Reynolds number of $Re_c = 9.36 \cdot 10^5$ based on the length c of the hump and at an inflow Mach number of $M_\infty = 0.1$. Similar to the backward facing step, the whole flow remains subsonic. Again, the required computational grids were taken from the NASA TMR-website [25]. For the computations presented here, the second finest grid consisting of 817×217 points and the finest grid consisting of 1633×433 points are applied.

In figure 3.10, the pressure coefficients and the skin-friction coefficients for both grids along the wall of the hump are shown. On the second finest grid, all three variants of

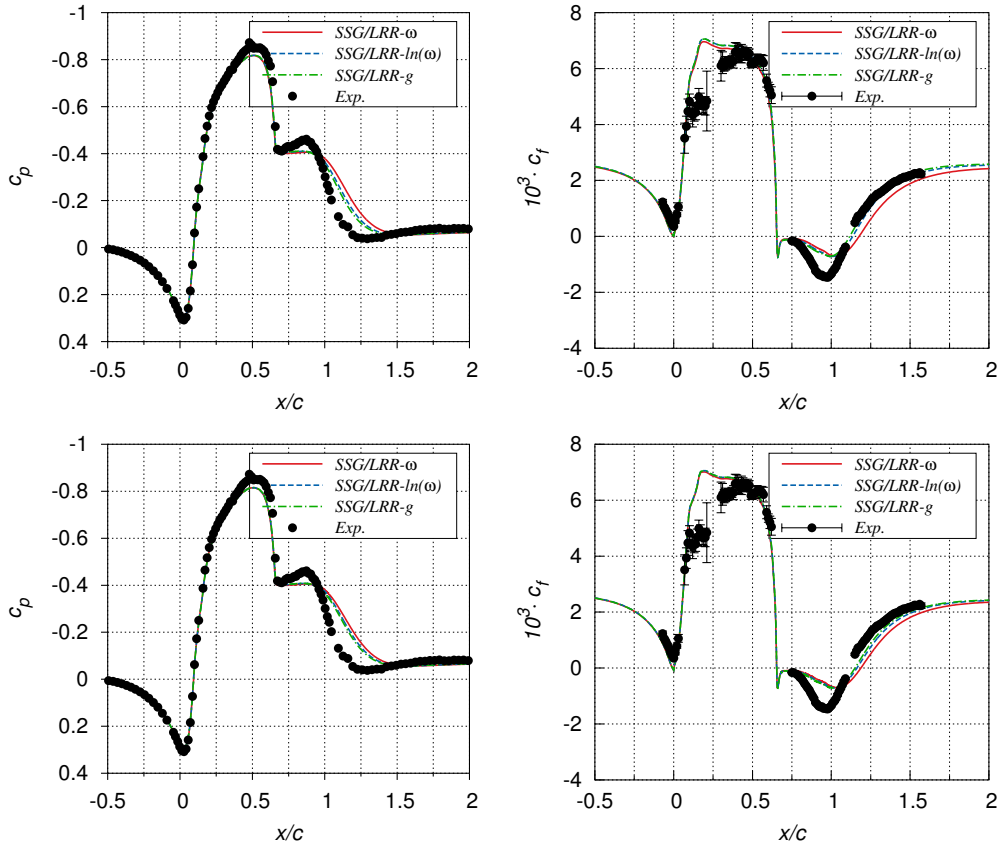

Figure 3.10: Comparison of the three SSG/LRR-variants for the NASA wall mounted hump on the second finest grid (817×217 points, top) and the finest grid (1633×433 points, bottom) [25]. Computations conducted at $M_\infty = 0.1$ and $Re_c = 9.36 \cdot 10^5$.

the SSG/LRR-RSM show differences in the pressure distribution on the wall below the separated flow ($0.6 < x/c < 1.2$). While the differences between the SSG/LRR-ln(ω) variant and the SSG/LRR-g version are small, larger deviations can be observed between these two variants and the original SSG/LRR-ω version. The main reason for these differences in the pressure distribution is the size of the separation bubble. The bubble size is indicated by the negative skin friction coefficients on the surface of the hump that can be found in the upper right plot. Both the ln(ω)-variant and the g-variant produce noticeable smaller separations. As both model versions are obtained by a pure mathematical transformation of the original model and therefore contain no additional physics, it is expected that the errors are caused by an insufficient spatial discretization and that the results would be identical on a finer grid. To verify this assumption, additional computations are carried out on the finest grid that contains four times the number of points. On this grid, the ln(ω)-version and the g-variant of the model predict almost identical values for c_P and c_f. Furthermore, the deviations to the original SSG/LRR-ω model become noticeable smaller as can be seen in the two plots in the lower part of figure 3.10. One possible reason for the remaining deviations could be a still insufficient spatial discretization of the additional gradient term that arises from the transformation of ω to ln(ω) (see equation 2.3) as well as from the transformation of ω to g [27]. Therefore, even finer grids may be required to obtain a solution that is identical for all three versions of the SSG/LRR-model.

3.2.5 DLR-F15 with a Spoiler

As the VitAM project in which this research was conducted focusses on the simulation of flight control systems, the DLR-F15 model with a spoiler statically deployed at $\delta = 30°$ is used as a final validation case. In contrast to the test cases presented in the preceding sections, the computations are conducted on a fully three-dimensional mesh. Furthermore, the flow is highly unsteady in this case due to a vortex shedding predicted downstream of the deployed spoiler. Therefore, time-accurate computations are carried out using a dual-time-stepping backward difference scheme [18]. In addition to the computation with the SSG/LRR-ln(ω) RSM, the SST model [21] and an explicit algebraic Reynolds stress model (EARSM) [17] are used. The computational mesh employed in this study contains 19.9 million grid points and was supplied by S. Geisbauer [13]. The computations are carried out at a Reynolds number of $Re_c = 2.6 \cdot 10^6$, at a reference Mach number of $M_\infty = 0.2$ and at an angle of attack of $\alpha = 0°$. Additional information about the numerical setup and the used mesh can be found in [13]. The experimental results shown in the subsequent figures are published in [15]. An overview of the geometry of the DLR-F15 spoiler configuration and the typical flow separation downstream of the spoiler is given in figure 3.11. The separation bubble in the wake of the spoiler is visualized in the right part of figure 3.11 by stream traces that are colored by the mean value of the x-velocity.

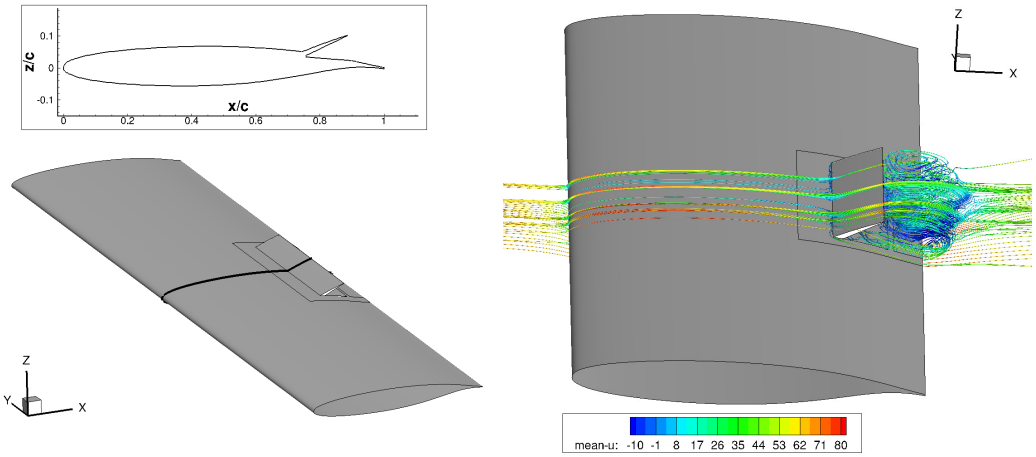

Figure 3.11: DLR-F15 model with a deployed spoiler. Left: overview of the geometry of the model. Right: stream traces (colored by the mean value of the x-velocity mean-u in m/s) visualizing the flow topology behind the spoiler. The mid-section of the model shown in the upper left section is marked by a black line in the lower left figure. Computations conducted at $M_\infty = 0.2$, $Re_c = 2.6 \cdot 10^6$, $\alpha = 0°$, $\delta = 30°$.

Due to the unsteady nature of the flow behind the spoiler, oscillations of the forces generated by the wing are observed. Therefore, the data for pressure and skin-friction shown in figure 3.12 are time-averaged. On the left side of figure 3.12, the pressure distribution computed with the three turbulence models on the mid-span section of the wing[2] are plotted against experimental data. All three turbulence models predict very similar pressure distributions and agree well with the experimental data, with the exception of the wake region behind the spoiler. Downstream of the spoiler, the EARSM model predicts the lowest pressure while the SST model predicts the highest one that is in closest agreement with the experimental data. The SSG/LRR-ln(ω) RSM delivers a c_p -distribution that is in between the results computed with the SST model and the results delivered by the EARSM model. Similar to the hump test case, the main reason for the deviations of the c_p -distribution in the wake region can be found in the differences of the sizes of the separation bubbles. As can be seen in the plot in the right part of figure 3.12, all three models deliver very similar c_f -level with slightly different locations of the reattachment points.

For the sake of completeness, time-averaged force coefficients and the pitching moment coefficient c_m for the complete wing are given in table 3.2.

[2] Compare figure 3.11.

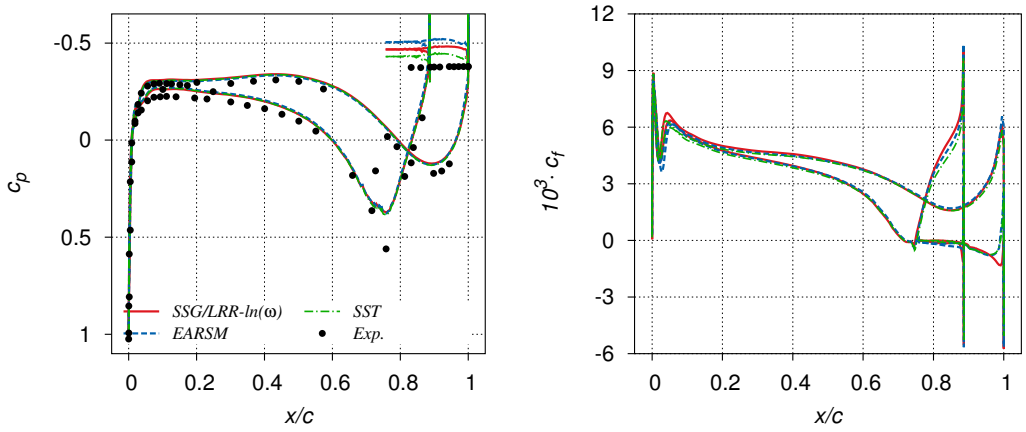

Figure 3.12: Time averaged surface pressure coefficients (left) and skin-friction coefficients (right) on the mid-section of the DLR-F15 model with a deployed spoiler. Computations conducted at $M_\infty = 0.2$, $Re_c = 2.6 \cdot 10^6$, $\alpha = 0°$, $\delta = 30°$.

turbulence model	c_L	c_d	c_m
SST	0.1414	0.02434	−0.06197
EARSM	0.1471	0.02597	−0.06399
SSG/LRR-ln(ω)	0.1354	0.02525	−0.061139

Table 3.2: Time-averaged force coefficients for the DLR-F15 spoiler test case. Computations conducted at $M = 0.2$, $Re_c = 2.6 \cdot 10^6$, $\alpha = 0°$, $\delta = 30°$.

4 Stability and Robustness

In order to evaluate how the new ln(ω)-version of the SSG/LRR model affects the robustness of the flow solver and the stability of the solution procedure, several competitive simulations with the new model variant and with the existing ones are performed. These investigations contain some of the basic test cases already presented in chapter 3 as well as configurations relevant for industry like the NASA Common Research Model [28] or the DLR-F11 high-lift configuration [24].

4.1 RAE 2822

In order to evaluate the robustness of the new model version in a transonic flow regime, the so called "Case 9" of the RAE 2822 airfoil test campaign [9] is used. In this campaign, the measurements were carried out at a chord based Reynolds number of $Re_c = 6.5 \cdot 10^6$ and at a Mach number of $M_\infty = 0.73$. The angle of attack was set to $\alpha = 2.8°$ during the test. In the computations conducted here, five computational meshes with a spatial resolution ranging from 11 112 (labeled grid-5) to 260 627 (labeled grid-1) grid points are used. In figure 4.1, the density residual (Rrho) is plotted against the number of conducted iterations. Using a CFL number of 15, the density residual is reduced by more than 13 orders of magnitude when the equations of the SSG/LRR-ln(ω) model are discretized with the four coarsest meshes. In contrast, the solution procedure stalls for the original SSG/LRR-ω model after a reduction of seven orders of magnitude at best and even crashes on the coarsest mesh. A very similar behavior can be observed when the finest mesh is used. The convergence history plotted in the right part of figure 4.1 shows that the solution procedure converges towards machine zero if the SSG/LRR-ln(ω) variant is used. In case of the original model formulation, the density residual starts to oscillate at Rrho $\approx 5 \cdot 10^{-5}$. Reducing the CFL number from 15 to 12 reduces the number of required iterations from several millions to merely 40 000 when the ln(ω)-variant is applied but does not fix the problem for the original model. In order to get a converged solution with the SSG/LRR-ω model, even smaller CFL-numbers are required.

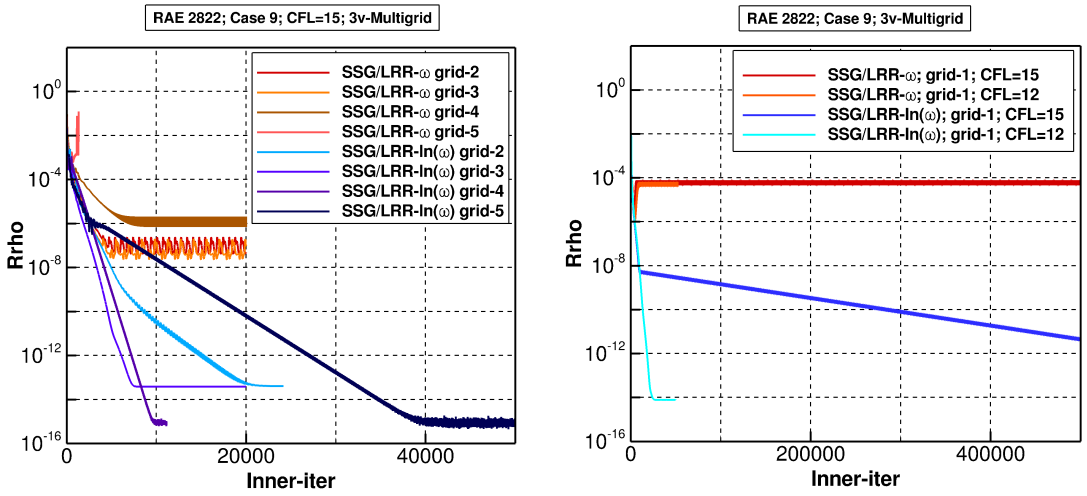

Figure 4.1: Convergence history for the RAE 2822 airfoil using the SSG/LRR-ω model and the SSG/LRR-ln(ω) variant on five different meshes: grid-5: 11 112 grid points, grid-1: 260 672 grid points. The number of points doubles in each refinement step. Flow conditions for Case 9: $Re_c = 6.5 \cdot 10^6$, $M = 0.73$, $\alpha = 2.8°$.

It has to be mentioned here, that the observed problems with the SSG/LRR-ω model don't originally arise from the investigated geometry or due to in any way challenging flow conditions but from the numerical setup used for the computations. Here, a three stage multigrid algorithm has been used and the computations were conducted on ten computational cores in parallel. Therefore, only a few grid points are processed by each core on the lowest multigrid stage especially in the cases in which the two coarsest meshes were used. When the number of used cores is reduced or the multigrid algorithm is switched of, a machine accurate solution can also been achieved with the SSG/LRR-ω model for CFL-numbers bigger than 10 without any problems. Nevertheless, this is not required for the SSG/LRR-ln(ω) variant. This behavior indicates that the SSG/LRR-ln(ω) variant is not only more robust in theory but also in practice.

4.2 2D Airfoil Near-Wake

Similar to the RAE 2822 airfoil, the Nakayama airfoil (see section 3.2.1) should pose no insurmountable difficulties to the flow solver. Nevertheless, computations using the unmodified SSG/LRR-ω model crashed. In contrast, the simulations can be conducted without problems after switching to the SSG/LRR-ln(ω) variant or the SSG/LRR-g variant of the

model. In figure 4.2, the convergence histories for the residuals of the density (Rrho), the residuals of the first normal component of the Reynolds stress tensor (Rrhor11) and the residuals of the length-scale determining variables (Rrholnw or Rrhog) are shown. Both model variants show a similar convergence behavior and no clear comparative advantage of one of the variants over the other can be found for the residuals of the density and the residual of the Reynolds stress component. Solely the residual of $In(\omega)$ drops somewhat faster than the residual of g during the initial phase of the computation.

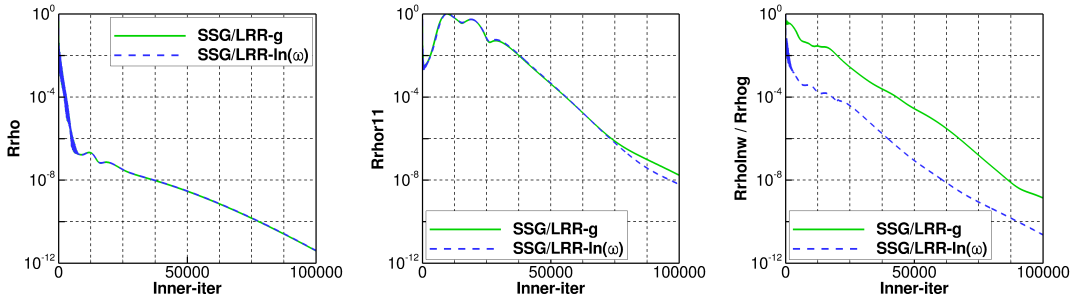

Figure 4.2: Convergence history for the Nakayama airfoil computed with the SSG/LRR-g RSM and the SSG/LRR-ln(ω) RSM. Information about the flow conditions and the used mesh can be found in section 3.2.1.

4.3 2D Backward facing step

The backward facing step test case poses a challenge to flow solvers as the separation bubble that exists in the wake of the step is prone to oscillations during the solution procedure especially when a Reynolds stress model is used. In order to get a converged steady solution with TAU, a very large number of iterations up to several millions as well as small CFL-numbers are required. In figure 4.3, the convergence histories for this test case delivered by the SSG/LRR-ω model and the SSG/LRR-ln(ω) variant for the residual of the density (Rrho), the residual of the first normal component of the Reynolds stress tensor (Rrhor11) and the residuals of the length-scale providing variables (Rrhow and Rrholnw) are shown. In this test case, no major improvement can be observed when the new $In(\omega)$-variant of the SSG/LRR model is used. There is no indication that the oscillations of the separation bubble are stabilized by changing the mathematical formulation of the length-scale determining variable from ω to $In(\omega)$.

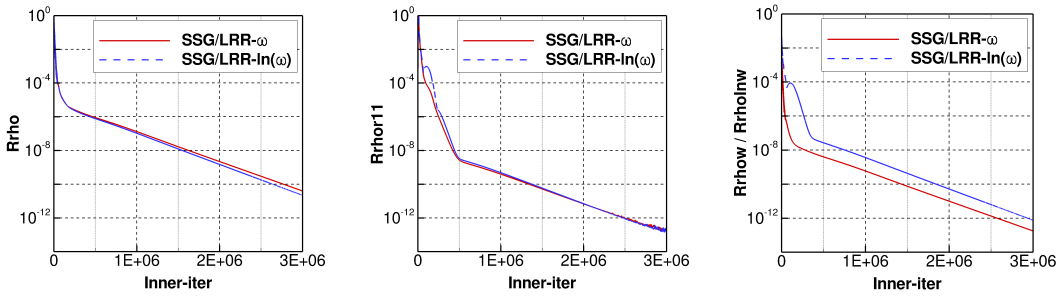

Figure 4.3: Convergence history for the backward facing step computed with the SSG/LRR-ω RSM and the SSG/LRR-ln(ω) RSM. Information about the flow conditions and the used mesh can be found in section 3.2.3.

4.4 Common Research Model

The NASA Common Research Model (CRM) [28] shown in figure 4.4 is used to perform stability and convergence tests with the three different versions of the SSG/LRR model for an industrial relevant 3D-application at transonic speeds. The used mesh was provided by NASA in the framework of the sixth AIAA drag prediction workshop [22]. Prisms are used within this mesh in order to discretize the boundary layers near viscous walls and tetrahedrons are used everywhere else. In total, the mesh contains 42.8 million grid points. The simulations are conducted at an angle of attack of $\alpha = 4°$ and at a Mach number of $M_\infty = 0.85$. In contrast to the model shown in figure 4.4, the through-flow nacelles are not present in the studies conducted here. Several simulations using a three stage multigrid approach are performed under the conditions described above with CFL-numbers in the

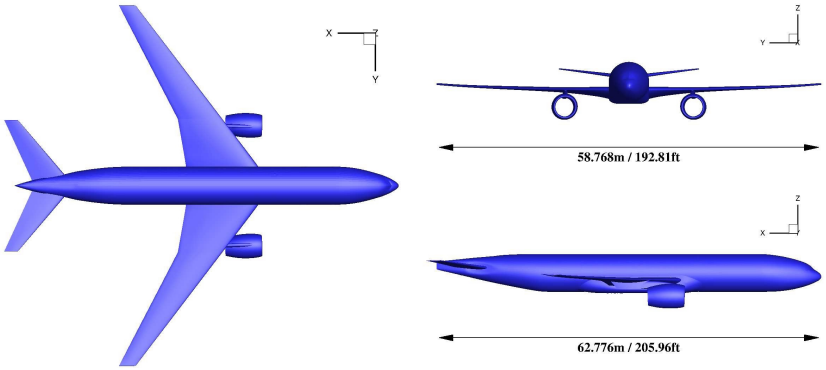

Figure 4.4: Scaled CAD model of the NASA Common research model. Adopted from [19].

range from 3 to 50[1]. The time integration is performed by using an implicit backward Euler scheme. The resulting convergence histories for the residual of the density (Rrho) and the residual of the Reynolds stress component R_{11} (Rrhor11) are shown in figure 4.5.

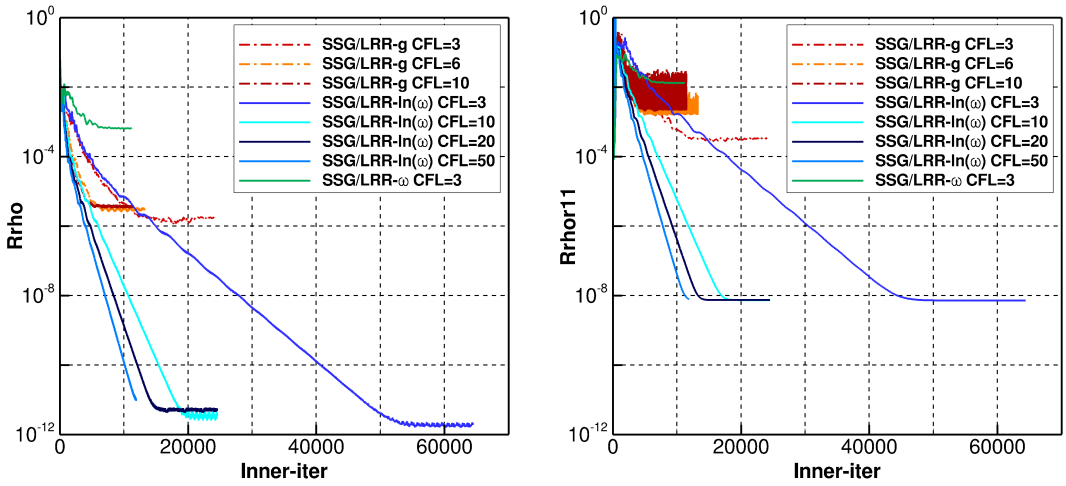

Figure 4.5: Convergence history for the NASA-CRM at $\alpha = 4°$, $Re_c = 5 \cdot 10^6$ and $Ma_\infty = 0.85$ computed with three different versions of the SSG/LRR RSM.

When using the SSG/LRR-ω model in combination with a CFL-number of 3, the density residual is reduced by merely three orders of magnitude before the solution procedure stalls. Deactivating the multigrid algorithm or a further reduction of the CFL-number does not improve this behavior. After switching from the SSG/LRR-ω model to the g-version, a much larger reduction of the density residual of more than five orders of magnitude can be observed. The residual of the Reynolds stresses is reduced by three orders of magnitude in case of the SSG/LRR-g model but less than a single order of magnitude when the original SSG/LRR-ω version is used. In order to check the stability limits of the SSG/LRR-g model, the CFL-number is increased in two steps from 3 to values of 6 and 10 respectively. Increasing the CFL-number divides the number of iterations required to achieve the same reduction of the density residual in halves. However, large oscillations of the residuals of the Reynolds stresses can be observed and the achievable convergence level is reduced to values bigger than 10^{-2}. Using the ln(ω)-formulation improves the convergence of the simulation remarkably. The density residual is reduced by almost twelve orders of magnitude independent of the used CFL-number. The same holds true for the residuals of the Reynolds stresses. There, a reduction to values of approximately 10^{-8} can be achieved. At this level, the solution procedure stalls as the limiter for the Reynolds stresses becomes

[1] In general, the given values refer to the CFL-numbers used on all levels of the multigrid algorithm. However, in the computations where a CFL-number of 3 is specified, the CFL-number on the coarse levels is further reduced to a value of CFL = 2.

active. Again, the CFL-number was increased in several steps in order to check the stability limits. No convergence issues or stability problems can be observed for CFL-numbers up to 50. Using such a large CFL-number reduces the costs of the simulation by about 70% as the number of required iterations decreases from more than 50 000 to less than 14 000.

4.5 DLR-F11

The DLR-F11 high-lift test case is used to investigate the influence of the ln(ω)-modification on the stability and robustness of the TAU solver in case of geometrically complex and aerodynamically challenging 3D-configurations. The DLR-F11 high-lift model was extensively studied in different configurations at several flow conditions in the second High-lift prediction workshop [24]. Here, the configurations with and without flap-track fairings are investigated at a Reynolds number of $Re = 15 \cdot 10^6$, a Mach number of $M_\infty = 0.175$ and at incidence angles ranging from $\alpha = 7°$ to $\alpha = 22.5°$. The test case without flap-track fairings is computed at a single angle of attack of $\alpha = 16°$ only. All computations are carried out on the grids with the medium resolution (Grid D) available on the website of the High-lift prediction workshop [24]. As all SSG/LRR variants show convergence issues when a 3v multigrid (MG) cycle is used, the computations are run with a 2v multigrid cycle initially. Later on, the multigrid algorithm is deactivated in order to reduce oscillations in the residuals and the force coefficients. The convergence histories for the residual of the density, the residual of the first normal component of the Reynolds stress tensor and the residuals of the length-scale providing variables are shown for the original SSG/LRR-ω model as well as for the SSG/LRR-ln(ω) variant in figure 4.6 for the test case without flap-track fairings. It is evident from the convergence histories plotted in this figure that with the SSG/LRR-ln(ω) variant a somewhat better convergence level can be achieved compared to the computations with the SSG/LRR-ω model. When the SSG/LRR-ω model is used, the density residual drops by about three orders of magnitude while a reduction of the residual of about four orders of magnitude can be achieved with the new ln(ω)-version. For the Reynolds stresses, similar differences in the achieved convergence levels can be observed. Furthermore, large oscillations in the residual of the length-scale providing variable can be observed when the original model is used that don't exist in the computations with the SSG/LRR-ln(ω) variant. It is assumed that these oscillations are triggered by the artificial limitation of the specific dissipation rate. Switching from multigrid to singlegrid computations does not change the convergence behavior of the simulations with the SSG/LRR-ω model while an additional improvement can be observed when the SSG/LRR-ln(ω) variant is used. Nevertheless, no converged solution can be found as the flow around the DLR-F11 model is highly unsteady by nature.

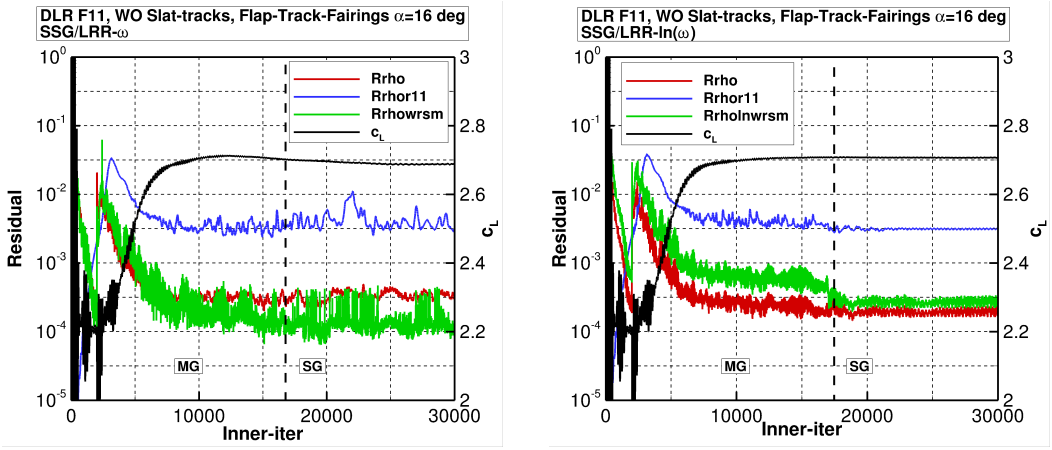

Figure 4.6: Convergence history for the DLR-F11 configuration without slat-track and flap-track fairings at $\alpha = 16°$ computed with the SSG/LRR-ω model (left) and the SSG/LRR-ln(ω) version (rigth) conducted at $M_\infty = 0.175$ and $Re = 15 \cdot 10^6$ on the Grid D [24].

For the DLR-F11 configuration with slat- and flap-track fairings, no results computed with the SSG/LRR-ω model can be presented here as all these computations crashed. Therefore, results from computations with the SSG/LRR-g model and the Spalart-Allmaras model (SA) are used for the comparison with the ln(ω)-variant of the SSG/LRR model in figure 4.7. Similar to the SA model and SSG/LRR-g model, no convergence issues are observed with the new model version. The polar computation starts at an incidence angle of $\alpha = 7°$ and is conducted up to an angle of $\alpha = 22.5°$ with a step size of $\Delta\alpha = 1°$. At large, no significant deviations between both SSG/LRR versions exist. Concerning the convergence history, the SSG/LRR-ln(ω) model delivers similar results as for the test case without flap-track fairing whereas the convergence histories of the computations that use the SSG/LRR-g model are very similar to the convergence history of the original SSG/LRR-ω model shown in the left part of figure 4.6.

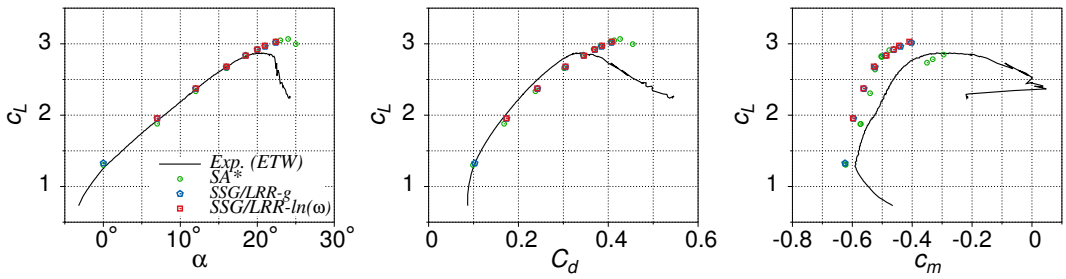

Figure 4.7: Force coefficients for the DLR-F11 configuration including slat- and flap-track fairings conducted at $M_\infty = 0.175$ and $Re = 15 \cdot 10^6$ on the medium size Grid D [24].

5 Summary

A new version of the SSG/LRR Reynolds stress model that uses the natural logarithm of the specific dissipation rate ω as the length-scale providing variable has been implemented into the DLR-TAU code. The derivation of the length-scale equation and the required boundary conditions were presented in chapter 2. A verification and a validation of the model implementation have been conducted using several test cases available from the NASA TMR-website [25]. These test cases covered wall bounded flows as well as separating flows. Provided that the used mesh is sufficiently refined, the newly implemented ln(ω)-version of the SSG/LRR RSM delivered the same results as the original SSG/LRR-ω model as well as identical results as its variant SSG/LRR-g. Based on the presented results, it can be concluded that the new model version has been implemented correctly into the flow solver TAU.

In addition, several competitive simulations with the new model version as well as with the existing ones have been carried out in order to evaluate how the ln(ω)-equation affects the robustness of the solver and the stability of the solution procedure. It has been shown that the convergence behavior of the ln(ω)-version of the SSG/LRR model is considerable better than that of the original SSG/LRR-ω model for some complex test cases as well as under unpropitious numerical setups. Furthermore, some advantages compared to the SSG/LRR-g model were observed. Especially, the large oscillations that can occur in the residual of the length-scale providing variable due to the artificial limitation of the variable can be avoided by using the ln(ω)-formulation. For simple test cases, no improvements were overserved when the new model version was applied.

Although some indications exist that the new ln(ω)-version of the SSG/LRR Reynolds stress model is more robust than the other model variants and can also improve the convergence behavior of RSM simulations in some cases, it has to be considered that the total number of computations conducted in this study was limited and the presented results are valid for the DLR-TAU solver only. Therefore, no general statement concerning a universal superiority of the new model version over the SSG/LRR-ω model or the SSG/LRR-g model can be made.

Acknowledgment

This research was conducted in the project VitAM (Advanced Aircraft Understanding via the Virtual Aircraft Model). The funding through the Federal Ministry for Economic Affairs and Energy under contract FKZ 20A1504A in the framework of the air transport research program LuFo IV is gratefully acknowledged. The results presented in this report have also been published in the milestone reports M-2.1-2 [3] and M-4.1-2 [5] of the VitAM project. The author thanks V. Togiti for conducting several of the verification and validation studies presented in chapter 3 and chapter 4 and for providing the required data as well as the corresponding plots and figures shown in this report. The supply of the mesh for the F15 spoiler test case by S. Geisbauer is also gratefully acknowledged.

Bibliography

[1] S. R. Allmaras, T. J. Forrester, and P. R. Spalart, "Modifications and Clarifications for the Implementation of the Spalart-Allmaras Turbulence Model", *7th International Conference on Computational Fluid Dynamics*, 2012.

[2] F. Bassi et al., "Discontinuous Galerkin solution of the Reynolds-averaged Navier-Stokes and k-ω turbulence model equations", *Computer & Fluids*, vol. 34, 2005.

[3] S. Braun, *Durch Anpassungen verbesserte, physikalische Modelle für abgelöste Strömungen abgeschlossen und integriert*, VitAM milestone report M-2.1-2, Institute of Aerodynamics and Flow Technolgy, DLR, 2017.

[4] S. Braun, *The concept of the SA-negative model and the application to ω-based turbulence models.* Interner Bericht DLR-IB-AS-BS-2017-3, ISSN 1614-7790, DLR, Institute of Aerodynamics and Flow Technology, Braunschweig, 2017.

[5] S. Braun and V. Togiti, *Angepasstes, verbessertes Turbulenzmodell für abgelöste Strömungen bewertet und validiert.* VitAM milestone report M-4.1-2, Institute of Aerodynamics and Flow Technology, DLR, 2018.

[6] S. Braun et al., "Numerical Simulation of Vortex Roll-up Processes using the SSG/LRR-ω Model", *New Results in Numerical and Experimental Fluid Mechanics X*, Springer-Verlag Berlin Heidelberg, 2016.

[7] O. Brodersen et al., "DLR Results from the Fourth AIAA Computational Fluid Dynamics Drag Prediction Workshop", *Journal of Aircraft*, 2012.

[8] R.-D. Cécora et al., "Differential Reynolds-Stress Modeling for Aerodynamics", *AIAA Journal*, vol. 53, no. 3, 2015.

[9] P. H. Cook, M. A. McDonald, and M. C. P. Firmin, *Aerofoil RAE2822 - Pressure Distributions and Boundary Layer and Wake Measurements*, AGARD advisory report AR-138, AGARD, 1979.

[10] D. M. Driver and H. L. Seegmiller, "Features of Reattaching Turbulent Shear Layer in Divergent Channel Flow", *AIAA Journal*, vol. 23, no. 2, 1985.

[11] B. Eisfeld, *Implementation of Reynolds Stress Models into the DLR-FLOWer Code*, tech. rep., ISSN 1614-7790, DLR, Institute of Aerodynamics and Flow Technology, Braunschweig, 2004.

[12] B. Eisfeld, C. Rumsey, and V. Togiti, "Verification and Validation of a Second-Moment-Closure Model", *AIAA Journal*, vol. 54, no. 5, 2016, pp. 1524–1541.

[13] S. Geisbauer, "Numerical simulation and validation of aerodynamics of static and dynamic spoilers", *Deutscher Luft- und Raumfahrtkongress (DLRK)*, 2018.

[14] S. Geisbauer, "Numerical Spoiler Wake Investigations at the Borders of the Flight Envelope", *29th AIAA Applied Aerodynamics Conference*, 2011.

[15] S. Geisbaur, and T. Loser, "Towards the Investigation of Unsteady Spoiler Aerodynamics", *AIAA Aviation Forum*, 2017.

[16] D. Greenblatt et al., "Experimental Investigation of Separation Control Part 1: Baseline and Steady Suction", *AIAA Journal*, vol. 44, no. 12, 2006, pp. 2820 –2830.

[17] A. Hellsten, "New Advanced k-ω Turbulence Model for High-Lift Aerodynamics", *AIAA Journal*, vol. 43, 2005, pp. 1857–1869.

[18] A. Jameson, "Time dependent calculations using multigrid, with applications to unsteady flows past airfoils and wings", *10th Computational Fluid Dynamics Conference, Fluid Dynamics and Co-located Conferences*, 1991.

[19] S. Keye, V. Togiti, and O. Brodersen, "DLR Results of the Sixth AIAA Computational Fluid Dynamics Drag Prediction Workshop", *55th AIAA Aerospace Sciences Meeting*, 2017.

[20] W. J. McCroskey, *A Critical Assessment of Wind Tunnel Results for the NACA 0012 Airfoil*, tech. rep. CP-429, AGARD, 1988.

[21] F. R. Menter, "Two-Equation Eddy-Viscosity Turbulence Models for Engineering Applications", *AIAA Journal*, vol. 32, 1994, pp. 1598–1605.

[22] J. H. Morrison, *6th AIAA CFD Drag Prediction Workshop.* 2016, URL: `https://aiaa-dpw.larc.nasa.gov`.

[23] A. Nakayama, "Characteristics of the Flow around Conventional and Supercritical Airfoils", *Journal of Fluid Mechanics*, vol. 160, 1985, pp. 155–179.

[24] C. L. Rumsey, *2nd AIAA CFD High Lift Prediction Workshop (HiLiftPW-2)*, 2016, URL: `https://hiliftpw.larc.nasa.gov`.

[25] C. L. Rumsey, *Turbulence Modeling Resource*, NASA, 2018, URL: `https://turbmodels.larc.nasa.gov`.

[26] P. R. Spalart and S. R. Allmaras, "A One-Equation Turbulence Model for Aerodynamic Flows", *30th Aerospace Sciences Meeting & Exhibition*, 1992.

[27] V. Togiti and B. Eisfeld, "Assessment of g-Equation Formulation for a Second-Moment Reynolds Stress Turbulence Model", *22nd AIAA Computational Fluid Dynamics Conference*, 2015.

[28] J. V. Vassberg et al., "Development of a Common Research Model for Applied CFD Validation Studies", *26th AIAA Applied Aerodynamics Conference*, 2008.

[29] D. C. Wilcox, *Turbulence Modelling for CFD*, 3rd ed., DCW Industries, Inc., 2006.